

Optical Conductivity of Topological Insulator Thin Films in a Quantizing Magnetic Field

A. Ullah and K. Sabeeh*

Department of Physics, Quaid-i-Azam University, Islamabad 45320, Pakistan.

Abstract

We determine the optical response of topological insulator thin films in the presence of a quantizing, external magnetic field. We explicitly take into account hybridization between the states of top and bottom surface. The interplay between hybridization and Zeeman energies gives rise to topological and normal insulator phases and phase transitions between them. The optical response in the two phases and at the phase transition point is investigated. We show that the difference in magneto-optical response can be used to distinguish the topological phase from the normal phase of the system. Further, the optical response also allows us to determine the gap generated by hybridization between top and bottom surface states of topological insulator thin films.

Pacs:

*Electronic address: ksabeeh@qau.edu.pk

I. INTRODUCTION

Three-dimensional (3D) Topological insulators (TIs) are materials that have a bulk bandgap but conducting surface states [1–4]. These materials usually have strong spin-orbit interaction. The conducting surface states are protected by time-reversal symmetry. The surface states have a linear dispersion relation and the quasiparticles (Dirac fermions) at the surface obey the massless Dirac equation. Further, the surface states are helical where intrinsic angular momentum (spin) and translational momentum are locked to each other with the Dirac cone centered at the time-reversal invariant momentum point in the Brillouin zone with spin polarized Berry phase[5–7]; which was confirmed by spin polarized Angle Resolved Photo Emission Spectroscopy (ARPES). These helical Dirac fermions exist on the edge of three-dimensional topological insulators such as Bi_2Se_3 , Bi_2Te_3 .

The gapless surface states are primarily responsible for transport in topological insulators. In transport studies of TIs, a major challenge is to separate the bulk contribution from the surface contribution. Since several TIs are layered materials, thin films can be synthesized with the advantage that thin films of topological insulators have minimum bulk contribution. Experiments on thin films are being actively pursued and it has been demonstrated that they exhibit thermoelectric effect[8], quantum spin Hall[9, 10], quantum anomalous Hall effect[11] and excitonic superfluidity[12]. Additionally, thin films provide an extra tunable degree of freedom which is their thickness. Thin films where states of top and bottom surfaces hybridize exhibit even richer physics. This hybridization can happen for 1-5 quintuple layers with a thickness of the order of $5nm$ [11, 13–16]. Fabrication of Bi_2Se_3 thin film by molecular beam epitaxy[13, 17] as well as its low temperature transport studies have been reported in[18]. Hybridization leads to opening the gap in the surface state dispersion[19]; in other words, it provides mass to Dirac fermions on the top and bottom surfaces. Further, this gap can be tuned by the application of an external magnetic field. It has been shown that the response of TI thin films in an external magnetic field is highly nontrivial[20–22]. TI thin films exhibit topological phases with phase transition that can be tuned by an external magnetic field. For surface state effects, the Fermi level has to be in the bulk band gap which can be controlled by doping a TI[5, 23] or by a gate potential. Another system that shares similarities with a TI thin film is bilayer graphene. At each valley, there are four parabolic bands in bilayer graphene, two valence and two conduction bands. Two of these

meet at the Charge Neutrality Point (CNP) exhibiting no energy gap in pristine bilayer; the remaining two are split from these. Gapless bilayer is a semi-metal but that can be changed. The gap can be opened and tuned by an electric field (gate potential) applied perpendicular to bilayer graphene sheets. This is in contrast to a TI thin film where there is a gap when the top and bottom surfaces are coupled and can be tuned by an applied magnetic field.

The main question that we address in this work is the effect of hybridization between top and bottom surface states on the magneto-optical response in thin film TIs. For this, we determine the complex frequency dependent longitudinal optical conductivity $\sigma(\omega)$; its real part gives the absorption as a function of photon energy. This has been carried out for graphene which shows good agreement between theory and experiment[24–28]. Recently in [29] optical properties of topological insulator thin films doped with magnetic impurities has been investigated. The authors include hybridization effects and for exchange field that breaks time reversal symmetry show that the value of Kerr and Faraday rotation angles is large for a wide range of frequencies. Magneto-optical properties of TIs[30] and other single layer material such as MoS_2 [31, 32] and silicene[33] have also been investigated. Landau levels are formed in the presence of an external magnetic field. Transitions between the Landau levels generate absorption lines in the magneto-optical conductivity[34, 35]. In [36, 37], these absorption lines were used to distinguish topological insulator phase and normal (band) insulator phase in silicene in the presence of spin orbit interaction and staggered potential. In this paper, we investigate topological phase transition in thin film of a topological insulator where hybridization between top and bottom surfaces is important. This will be done on the basis of information obtained from magneto-optical absorption spectra. We obtain the absorption spectra in both topological insulator phase and normal insulator phase as well as at the Charge Neutrality Point (CNP).

This paper is organized as follows: In section 2 and 3 we develop the theoretical model of a thin film topological insulator in a uniform external magnetic field. In section 4, we determine the longitudinal conductivity and transverse hall conductivity. In section 5, response to circularly polarized light is considered. In section 6, the topological phase transition in the semiclassical limit is investigated. In section 7 and 8, effect of broken inversion symmetry and effect of warping in thin film topological insulator on Landau levels has been discussed.

II. THEORY OF TOPOLOGICAL INSULATOR THIN FILM IN AN EXTERNAL MAGNETIC FIELD

We consider the Hamiltonian for the surface states in a topological insulator thin film aligned in the xy -plane with hybridization between the surface states. When thin film is subjected to transverse magnetic field $\mathbf{B} = \nabla \times \mathbf{A}$, Landau levels with quantized energies develop in the valence and conduction bands. We employ the minimal substitution $\mathbf{p} \rightarrow \mathbf{p} + \frac{e}{c}\mathbf{A}$ in the Landau gauge for vector potential $\mathbf{A} = (0, xB, 0)$ and c is the speed of light. The Hamiltonian of our system takes the form[11]:

$$\hat{H}_{\sigma\tau} = v_f \left[\sigma_x \left(p_y + \frac{eB}{c}x \right) - \tau_z \sigma_y p_x \right] + (\Delta_Z \tau_z + \Delta_H) \sigma_z. \quad (1)$$

Here $(\sigma_x, \sigma_y, \sigma_z)$ define Pauli matrices acting on real spin space. $\tau_z = +/ -$ represent the symmetric/antisymmetric linear combination of surface states represented by $|\tau_z \uparrow (\downarrow)\rangle = 1/\sqrt{2}(|t \uparrow (\downarrow)\rangle + \tau_z |b \uparrow (\downarrow)\rangle)$ [11]. Here t represents the top surface and b the bottom surface of the thin film. v_f is the Fermi velocity of Dirac fermions on the surface. Moreover, we have Zeeman energy $\Delta_Z = g\mu_B B/2$, the effective Lande factor g , the Bohr magneton μ_B , and Δ_H represents the hybridization contribution which is due to the hybridization between upper and lower surfaces of the TI. As p_x and x do not commute, we can write the Hamiltonian in terms of dimensionless operators

$$\hat{H}_{\sigma\tau} = \frac{v_f}{l_B} \left[\sigma_x l_B \hat{P} + \tau_z \sigma_y \frac{\hat{Q}}{l_B} \right] + (\Delta_Z \tau_z + \Delta_H) \sigma_z, \quad (2)$$

where $l_B = \sqrt{c/eB}$ is the magnetic length. $\hat{Q} = -l_B^2 p_x$ and $\hat{P} = p_y + \frac{eB}{c}x$ such that $[\hat{Q}, \hat{P}] = i\hbar$. Employing the ladder operators $a = 1/\sqrt{2\hbar}l_B(\hat{Q} + il_B^2 \hat{P})$ and $a^\dagger = 1/\sqrt{2\hbar}l_B(\hat{Q} - il_B^2 \hat{P})$, we may express the Hamiltonian as

$$\hat{H}_{\sigma\tau} = \sqrt{\frac{\hbar}{2}} \frac{v_f}{l_B} (i\sigma_x (a^\dagger - a) + \tau_z \sigma_y (a + a^\dagger)) + (\Delta_Z \tau_z + \Delta_H) \sigma_z. \quad (3)$$

which can also be written as

$$\hat{H}_{\tau_z=+1} = \begin{pmatrix} (\Delta_Z + \Delta_H) & -i\sqrt{2\hbar} \frac{v_f}{l_B} a \\ i\sqrt{2\hbar} \frac{v_f}{l_B} a^\dagger & -(\Delta_Z + \Delta_H) \end{pmatrix} \quad (4)$$

$$\hat{H}_{\tau_z=-1} = \begin{pmatrix} -(\Delta_Z - \Delta_H) & i\sqrt{2\hbar} \frac{v_f}{l_B} a^\dagger \\ -i\sqrt{2\hbar} \frac{v_f}{l_B} a & (\Delta_Z - \Delta_H) \end{pmatrix} \quad (5)$$

The energy of the Landau levels (LLs) is given by

$$E_n^{\tau_z} = \text{sgn}(n) \sqrt{2\hbar v_f^2 e B |n| + (\Delta_Z + \tau_z \Delta_H)^2}, \quad (6)$$

$$E_0^{\tau_z} = -(\Delta_Z + \tau_z \Delta_H). \quad (7)$$

$\omega_B = v_f/l_B$ is the cyclotron frequency of Dirac fermions. $n = 0, \pm 1, \pm 2, \dots$ is the Landau level index. An important feature of the energy spectrum is the splitting of $n \neq 0$ Landau levels for non-zero value of Zeeman energy and hybridization between top and bottom surface states. This splitting of $n \neq 0$ requires both Zeeman energy and hybridization to be nonzero. Further, the energy spectrum is electron-hole symmetric in the absence of Zeeman energy ($\Delta_Z = 0$). For $\Delta_z < \Delta_H$ with a finite hybridization gap, it is not strictly electron-hole symmetric; the $n \neq 0$ spectrum maintains this symmetry where as $n = 0$ spectrum does not. Note that a quadratic term can appear in the Hamiltonian even in the absence of both Zeeman energy and hybridization[38], if there is no electron-hole symmetry, as shown by angle resolved photoemission spectroscopy. In our case we have not considered a quadratic term in Eq. (1) as it can be neglected when the system is doped such that the Dirac point is close to the charge neutrality point (CNP), which is the focus of our work. The $n = 0$ Landau level splits only when Δ_H is nonzero. The LL energy spectrum carries important information regarding topological phase transition in the system. The $n = 0$ Landau level E_0^- changes sign during the phase transition from normal insulator ($\Delta_z < \Delta_h$) to topological insulator ($\Delta_z > \Delta_h$). For normal insulator phase E_0^- is hole like and for topological insulator phase it is electron like. This represents an extra filled Landau level which gives rise to Hall conductivity e^2/h [20]; hence we can write

$$\sigma_{xy} = \frac{e^2}{2h} (\text{sgn}(\Delta_Z - \Delta_H) + 1). \quad (8)$$

At $\Delta_Z = \Delta_H$, E_0^- has exactly zero energy and is at the charge neutrality point (CNP). If the chemical potential is tuned to CNP, this zeroth Landau level will be partially filled. The plot of Landau levels with respect to magnetic field is shown in Fig. 1 with $g = 60$ and $\mu_B = 5.788 \times 10^{-6} \frac{eV}{T}$. Similar to graphene all $n \neq 0$ Landau levels scale as \sqrt{B} . But unlike graphene $n = 0$ Landau levels do not sit at zero energy when $\Delta_Z \neq \Delta_H$. The energy of one of the $n = 0$ Landau levels becomes zero for $\Delta_Z = \Delta_H$. At that point $\Delta_H = 4meV$ with magnetic field $B = 2.3T$. This represents the topological phase as shown in Fig. 1.

Using Eq. (4) and Eq. (5), the eigenvectors for symmetric surface states are

$$|\tilde{n}\rangle_{\tau_z=+1} = \begin{pmatrix} A_n |n|-1\rangle \\ B_n |n\rangle \end{pmatrix}, \quad (9)$$

and

$$|\tilde{n}\rangle_{\tau_z=-1} = \begin{pmatrix} A_n |n\rangle \\ B_n |n|-1\rangle \end{pmatrix},$$

where $|n\rangle$ is an orthonormal Fock state of the harmonic oscillator and

$$A_n = \begin{cases} \frac{1}{\sqrt{2}} \left(1 + \text{sgn}(n) \frac{(\Delta_Z + \tau_z \Delta_H)}{|E_n^{\tau_z}|}\right)^{1/2}, & n \neq 0, \\ 0, & n = 0, \end{cases} \quad (10)$$

and

$$B_n = \begin{cases} \frac{1}{\sqrt{2}} \left(1 - \text{sgn}(n) \frac{(\Delta_Z + \tau_z \Delta_H)}{|E_n^{\tau_z}|}\right)^{1/2}, & n \neq 0, \\ 1, & n = 0. \end{cases} \quad (11)$$

III. DENSITY OF STATES

To shed further light on the energy spectrum of our system, we determine the Dirac fermion density of states. The Green's function associated with our Hamiltonian is

$$G(\omega, n, \tau_z) = \sum_{\tau_z} \frac{1}{\omega - \text{sgn}(n) \sqrt{2v_f^2 \hbar e B |n| + (\Delta_Z + \tau_z \Delta_H)^2} + i\eta} \quad (12)$$

From which we can compute the density of states $D(\omega)$ as

$$D(\omega) = -\frac{1}{2\pi^2 l_B} \left[\sum_{n=-\infty}^{\infty} \sum_{\tau_z} \text{Im} G(\omega, n, \tau_z) \right] \quad (13)$$

which can be expressed as

$$D(\omega) = \frac{-1}{\pi} \frac{1}{2\pi l_B^2} \left[\sum_{\substack{n=-\infty \\ n \neq 0}}^{\infty} \sum_{\tau_z} \text{Im} G(\omega, n, \tau_z) + \sum_{\tau_z} \text{Im} G(\omega, 0, \tau_z) \right]. \quad (14)$$

This yields

$$D(\omega) = \frac{1}{2\pi l_B^2} \left[\sum_{\substack{n=-\infty \\ n \neq 0}}^{\infty} \sum_{\tau_z} \delta(\omega - \text{sgn}(n) \sqrt{2v_f^2 \hbar e B |n| + (\Delta_Z + \tau_z \Delta_H)^2}) + \sum_{\tau_z} \delta(\omega + (\Delta_Z + \tau_z \Delta_H)) \right] \quad (15)$$

The plot of density of states $D(\omega)$ is shown in Fig. 2 as a function of energy. We used $B = 1T$ and $\eta = 0.12\Delta_H$; η is the scattering rate which results in broadening of the states. The two $n = 0$ Landau levels are located at $\omega = -(\Delta_Z + \Delta_H)$ and $\omega = -(\Delta_Z - \Delta_H)$. At $\Delta_Z = \Delta_H$ we have peak at CNP representing partial filled Landau level. Peak at CNP shifts to the hole region by increasing Zeeman energy or it shifts to the electron region by decreasing Zeeman energy relative to the hybridization as shown in Fig. 2(a) and 2(c).

IV. MAGNETO-OPTICAL CONDUCTIVITY

We determine the magneto-optical conductivity with in the linear response regime using the Kubo formula[28, 39]

$$\sigma_{\alpha\beta} = \frac{i}{2\pi l_B^2} \sum_{\tau_z=\pm 1} \sum_{nm} \frac{f_m - f_n}{(\varepsilon_n - \varepsilon_m)} \frac{\langle \tilde{m} | \hat{j}_\alpha | \tilde{n} \rangle \langle \tilde{n} | \hat{j}_\beta | \tilde{m} \rangle}{\hbar\omega + \varepsilon_m - \varepsilon_n + i\eta}, \quad (16)$$

where $\hat{j}_\alpha = e \frac{\partial H}{\partial k_\alpha}$ and $f_m = 1/[1 + \exp(\beta(\varepsilon_m - \mu))]$ is the Fermi distribution function with $\beta = 1/k_B T$, ε_m is the energy of m th Landau level and η is scattering rate taken as constant. We will take states m to be occupied and n as unoccupied LLs. The selection rule for Landau levels transition is $|n| = |m| \pm 1$ determined by the evaluation of matrix elements. At zero temperature we can drop the absolute value of n and all transition to negative Landau levels are Pauli blocked. For longitudinal magneto-optical conductivity with $\hat{j}_x = ev_f(-\tau_z \sigma_y)$, the matrix element for symmetric eigenstates is determined as

$$\langle |\tilde{m}| | \hat{j}_x | \tilde{n} \rangle \langle \tilde{n} | \hat{j}_x | |\tilde{m}| \rangle = v_f^2 e^2 [(A_m B_n)^2 \delta_{|m|-1,n} + (A_n B_m)^2 \delta_{|m|+1,n}], \quad (17)$$

and for antisymmetric eigenstates, it is

$$\langle |\tilde{m}| | \hat{j}_x | \tilde{n} \rangle \langle \tilde{n} | \hat{j}_x | |\tilde{m}| \rangle = v_f^2 e^2 [(A_m B_n)^2 \delta_{|m|-1,n} + (A_n B_m)^2 \delta_{|m|+1,n}]. \quad (18)$$

Therefore, we obtain

$$\frac{\sigma_{xx}}{\sigma_o} = \frac{2iv_f^2 e \hbar B}{\pi} \sum_{\tau_z=\pm 1, mn} \frac{[(A_m B_n)^2 \delta_{n,|m|-1} + (A_n B_m)^2 \delta_{n,|m|+1}]}{(E_n^{\tau_z} - E_m^{\tau_z})(\hbar\omega + E_m^{\tau_z} - E_n^{\tau_z} + i\eta)}. \quad (19)$$

where $\sigma_o = e^2/4\hbar$. From the above result it is clear that for possible transitions we must have $n = |m| \pm 1$. Using the selection rule $n = |m| \pm 1$ we can write

$$\frac{\sigma_{xx}(\omega)}{\sigma_o} = \frac{2iv_f^2 e\hbar B}{\pi} \sum_{\tau_z = \pm 1, m} \left[\frac{(A_{|m|+1} B_m)^2}{(E_{|m|+1}^{\tau_z} - E_m^{\tau_z})(\hbar\omega + E_m^{\tau_z} - E_{|m|+1}^{\tau_z} + i\eta)} + \frac{(A_m B_{|m|-1})^2}{(E_{|m|-1}^{\tau_z} - E_m^{\tau_z})(\hbar\omega + E_m^{\tau_z} - E_{|m|-1}^{\tau_z} + i\eta)} \right] \quad (20)$$

$$\frac{\text{Re } \sigma_{xx}(\omega)}{\sigma_o} = \frac{2v_f^2 e\hbar B}{\pi} \sum_{\tau_z = \pm 1, m} \left[\frac{[(A_{|m|+1} B_m)^2 \times \eta]}{(E_{|m|+1}^{\tau_z} - E_m^{\tau_z})[(\hbar\omega + E_m^{\tau_z} - E_{|m|+1}^{\tau_z})^2 + \eta^2]} + \frac{(A_m B_{|m|-1})^2 \times \eta}{(E_{|m|-1}^{\tau_z} - E_m^{\tau_z})[(\hbar\omega + E_m^{\tau_z} - E_{|m|-1}^{\tau_z})^2 + \eta^2]} \right] \quad (21)$$

For transverse Hall conductivity $\hat{j}_x = ev_f(-\tau_z \sigma_y)$ and $\hat{j}_y = ev_f(\sigma_x)$. The matrix elements are evaluated to yield

$$\frac{\sigma_{xy}}{\sigma_o} = \frac{2v_f^2 e\hbar B}{\pi} \sum_{\tau_z = \pm 1, mn} \frac{\tau_z [(A_n B_m)^2 \delta_{n,|m|+1} - (A_m B_n)^2 \delta_{n,|m|-1}]}{(E_n^{\tau_z} - E_m^{\tau_z})(\hbar\omega + E_m^{\tau_z} - E_n^{\tau_z} + i\eta)} \quad (22)$$

Using selection rule $n = |m| \pm 1$ we can write

$$\frac{\sigma_{xy}}{\sigma_o} = \frac{2v_f^2 e\hbar B}{\pi} \sum_{\tau_z = \pm 1, m} \left[\frac{\tau_z [(A_{|m|+1} B_m)^2]}{(E_{|m|+1}^{\tau_z} - E_m^{\tau_z})(\hbar\omega + E_m^{\tau_z} - E_{|m|+1}^{\tau_z} + i\eta)} - \frac{\tau_z (A_m B_{|m|-1})^2}{(E_{|m|-1}^{\tau_z} - E_m^{\tau_z})(\hbar\omega + E_m^{\tau_z} - E_{|m|-1}^{\tau_z} + i\eta)} \right] \quad (23)$$

This is the general expression for transverse Hall conductivity representing transition from m to $|m| \pm 1$ state. We can also determine $\text{Im } \sigma_{xy}/\sigma_o$ as

$$\frac{\text{Im } \sigma_{xy}}{\sigma_o} = \frac{2v_f^2 e\hbar B}{\pi} \sum_{\tau_z = \pm 1, m} \left[\frac{-\tau_z (A_{|m|+1} B_m)^2 \times \eta}{(E_{|m|+1}^{\tau_z} - E_m^{\tau_z})[(\hbar\omega + E_m^{\tau_z} - E_{|m|+1}^{\tau_z})^2 + \eta^2]} + \frac{\tau_z (A_m B_{|m|-1})^2 \times \eta}{(E_{|m|-1}^{\tau_z} - E_m^{\tau_z})[(\hbar\omega + E_m^{\tau_z} - E_{|m|-1}^{\tau_z})^2 + \eta^2]} \right]. \quad (24)$$

Fig. 3(c) shows $\text{Re } \sigma_{xx}(\omega)/\sigma_o$ as a function of frequency in normal insulator phase showing absorption line for interband transitions with $v_f^2 e\hbar B = 1.6 \times 10^{-4}$ for magnetic field of 1 Tesla and $\mu = 0$. The transition energy is determined from the energy gap between Landau levels satisfying the selection rule for allowed transitions. The first two absorption peaks correspond to $E_{-1}^- \rightarrow E_0^-$ and $E_0^+ \rightarrow E_1^+$ transitions. These transitions involve zeroth

Landau level. The energy of first peak is $E_0^- - E_{-1}^-$ and for the second peak it is $E_1^+ - E_0^+$. Each of these peaks represents single transition. The absorption peaks for allowed transitions which involve Landau levels other than $E_0^{\tau_z}$ represent the sum of absorption peaks of two transitions in the absence of hybridization ($\Delta_H = 0$), one transition for $E_{-n} \rightarrow E_{n+1}$ and another transition for $E_{-(n+1)} \rightarrow E_n$. However, for finite hybridization Δ_H , each peak splits into two peaks for $\tau_z = +1$ and $\tau_z = -1$. First peak represents $E_{-n}^{-1} \rightarrow E_{n+1}^{-1}$ and $E_{-(n+1)}^{-1} \rightarrow E_n^{-1}$ transitions. The second peak represents $E_{-n}^{+1} \rightarrow E_{n+1}^{+1}$ and $E_{-(n+1)}^{+1} \rightarrow E_n^{+1}$ transitions. For a fixed hybridization, the splitting between these peaks depends on the applied magnetic field; the energy gap is $(\Delta_Z + \tau_z \Delta_H)$. Further, the spacing between absorption peaks also depends on the broadening parameter η ; we have taken its value to be $\eta = 0.15\Delta_H$ estimated from experimental findings[40]. Moreover, at low magnetic fields, in the NI phase, the splitting between $\tau_z = -1$ and $\tau_z = -1$ is very small as shown in Fig. 3(c). Fig. 3(b) shows the real part of $\sigma_{xx}(\omega)$ at CNP. For the 1st peak two transitions, represented by arrows, $E_0^- \rightarrow E_1^-$ and $E_{-1}^- \rightarrow E_0^-$ contribute. While 2nd peak represents $E_0^+ \rightarrow E_1^+$ transition. The value of Zeeman interaction is large enough that it can open a gap between LLs of different τ_z but same Landau index n resulting in splitting of absorption peaks; this is clearly seen in 3rd peak. Fig. 3(a) shows $\text{Re } \sigma_{xx}(\omega)/\sigma_o$ as a function of frequency in the topological insulator phase with broken particle-hole symmetry for interband transitions. The first absorption peak represents the transition $E_0^- \rightarrow E_1^-$, while the second peak represents the $E_0^+ \rightarrow E_1^+$ transition. An important feature of the absorption spectra is that the $E_0^- \rightarrow E_1^-$ has replaced the $E_{-1}^- \rightarrow E_0^-$ transition which was allowed in normal insulator phase but Pauli blocked in topological insulator phase. Another difference arises in absorption peaks for topological insulator phase when Δ_Z is large. The large value of Δ_Z induces significant gap between $\tau_z = +1$ and $\tau_z = -1$ Landau levels of same n . The effect of this gap can be seen in the absorption peaks for $\text{Re } \sigma_{xx}(\omega)/\sigma_o$. The splitting in the peaks is significant as compared to normal insulator phase of same τ_z . Each peak in the pair has same transition energy for the transition $m \rightarrow |m| \pm 1$ with same τ_z . For example, the third absorption peak is the sum of two peaks resulting from the $E_{-1}^- \rightarrow E_2^-$ and $E_{-2}^- \rightarrow E_1^-$ transition with same energy. Similarly the fourth peak represents sum of $E_{-1}^+ \rightarrow E_2^+$ and $E_{-2}^+ \rightarrow E_1^+$ transitions.

The absorption peaks obtained from $\text{Im } \sigma_{xy}(\omega)/\sigma_o$ have significant differences for the two phases. Fig. 4(c) represents the absorption peak for normal insulator phase. The first two peaks represent the absorption peaks for $\text{Im } \sigma_{xy}(\omega)/\sigma_o$ resulting from the $E_{-1}^- \rightarrow E_0^-$ and

$E_0^+ \rightarrow E_1^+$ transitions. It shows same behavior as for $\text{Re}\sigma_{xx}(\omega)/\sigma_o$ in the normal insulator phase. The other peaks show different behavior. In Eq. (24) for $\text{Im}\sigma_{xy}(\omega)/\sigma_o$ the transition $m \rightarrow |m| + 1$ with $\tau_z = +1$ has positive amplitude and for $m \rightarrow |m| - 1$ with $\tau_z = +1$ the amplitude is negative. Similarly for $\tau_z = -1$ the transition $m \rightarrow |m| + 1$ and $m \rightarrow |m| - 1$ has negative and positive amplitudes respectively. These differences not only decrease the height of absorption peaks but they also create oscillations in absorption peaks for $\text{Im}\sigma_{xy}(\omega)/\sigma_o$ in the topological insulator phase. For example the terms for the first peak in Eq. (24) for $\tau_z = -1$ have $E_{-1}^- \rightarrow E_2^-$ and $E_{-2}^- \rightarrow E_1^-$ transitions. Both of these transitions have opposite signs but have same transition energy. So these terms decrease the height of absorption peaks. Similar behavior is seen for $\tau_z = +1$. The amplitude for the transition with $m \rightarrow |m| + 1$ with $\tau_z = +1$ will always be greater than the amplitude of transition $m \rightarrow |m| - 1$ for $\tau_z = -1$ in both topological insulator and normal insulator phase. At CNP, the contribution to absorption peak in $\text{Im}\sigma_{xy}(\omega)/\sigma_o$ resulting from transitions involving $\tau_z = -1$ LLs are absent. At $\Delta_Z = \Delta_H$ all transitions resulting from $\tau_z = -1$ cancel out and the contribution to absorption peaks is given by transition between Landau levels with $\tau_z = +1$. The first peak in Fig. 4(b) represents the transition $E_0^+ \rightarrow E_1^+$ while for the 2nd case two transitions contribute *i.e.* $E_{-1}^+ \rightarrow E_2^+$ and $E_{-2}^+ \rightarrow E_1^+$, transitions. Fig. 4(a) represents the absorption peaks for $\text{Im}\sigma_{xy}(\omega)/\sigma_o$ in TI phase. At $\Delta_Z > \Delta_H$ the absorption peaks has negative and positive peaks. The first negative peak results from the transition $E_0^- \rightarrow E_1^-$, while the second positive peak represent the $E_0^+ \rightarrow E_1^+$ transition.

A schematic diagram which helps us to understand the behavior of the absorption lines that we have described is shown in Fig. 5 for NI, in Fig. 6 at CNP and in Fig. 7 in TI phase. On the left side we shown the Landau index n with energy define by Eq. (6). The blue lines represent the LLs with $\tau_z = -1$ while red lines represent LLs for $\tau_z = +1$. The bold black line gives the possible values of chemical potential $\mu = 0$. The possible optical transitions are indicated by vertical arrows and they connect the levels m to $|m| \pm 1$ only. Moving from left to right in Fig. 5 in NI phase we see first two single transition with different transition energy from E_{-1}^- to E_0^- and E_0^+ to E_1^+ , then a pair of interband transitions from E_{-1}^- to E_2^- and E_{-2}^- to E_1^- followed by another pair E_{-1}^+ to E_2^+ and E_{-2}^+ to E_1^+ . The difference between the transition energy of these two pairs is very small in NI phase showing small splitting in absorption peak of $\text{Re}\sigma_{xx}(\omega)/\sigma_o$. For TI the schematic of allowed transitions is shown in Fig. 7. The main difference in the TI and NI phase arises in the first transition.

The transition E_{-1}^- to E_0^- in NI is replaced by the transition E_0^- to E_1^- in TI. The 2nd transition is from E_0^+ to E_1^+ . It is followed by a pair of transitions from E_{-1}^- to E_2^- and E_{-2}^- to E_1^- followed by another pair E_{-1}^+ to E_2^+ and E_{-2}^+ to E_1^+ . The absorption peaks of the two pairs are well separated in the response function of $\text{Re}\sigma_{xx}(\omega)/\sigma_o$ as shown in Fig. 3(a). At CNP, the allowed transition are shown in Fig. 6. The first two transition involve partially filled Landau level E_0^- . These transition are E_0^- to E_1^- and E_{-1}^- to E_0^- . These have same transition energy. These transitions are followed by E_0^+ to E_1^+ , then pair of transitions same as describe previously. Fig. 8 and Fig. 9 represent $\text{Re}\sigma_{xx}(\omega)/\sigma_o$ resulted from allowed transitions in NI and TI phases respectively for $\mu = 0.02eV$. The red peak represents the absorption lines contributed by intraband transitions. While the black peaks represent the allowed interband transition splited in TI phase at high magnetic field. A schematic diagram for allowed transition with nonzero value chemical potential is shown in Fig. 10 for low magnetic field (NI) and in Fig. 11 for high magnetic field (TI) showing inter and intra band transitions.

V. CIRCULARLY-POLARIZED LIGHT

For circularly Polarized light the conductivity is written as $\sigma_{xx}(\omega) \pm i\sigma_{xy}(\omega)$ with (+) representing the right handed polarization and (-) representing left handed polarization. The circularly polarized light shows different behavior in normal insulator and in topological insulator phase. The absorptive part of conductivity is

$$\text{Re } \sigma_{\pm} = \text{Re } \sigma_{xx}(\omega) \mp \text{Im } \sigma_{xy}(\omega) \quad (25)$$

For normal insulator

$$\frac{\text{Re } \sigma_+(\omega)}{\sigma_o} = \frac{2v_f^2 e \hbar B}{\pi} \sum_{m=1}^{\infty} \left[\frac{[(A_{|m|+1} B_m)^2 \times \eta]}{(E_{|m|+1}^- - E_m^-)(\hbar\omega + E_m^- - E_{|m|+1}^-)^2 + \eta^2)} + \frac{(A_m B_{|m|-1})^2 \times \eta}{(E_{|m|-1}^+ - E_m^+)(\hbar\omega + E_m^+ - E_{|m|-1}^+)^2 + \eta^2)} \right] \quad (26)$$

and

$$\text{Re } \sigma_-(\omega) = \frac{2v_f^2 e \hbar B}{\pi} \sum_{m=0}^{\infty} \left[\frac{[(A_{|m|+1} B_m)^2 \times \eta]}{(E_{|m|+1}^+ - E_m^+)(\hbar\omega + E_m^+ - E_{|m|+1}^+)^2 + \eta^2)} + \frac{(A_m B_{|m|-1})^2 \times \eta}{(E_{|m|-1}^- - E_m^-)(\hbar\omega + E_m^- - E_{|m|-1}^-)^2 + \eta^2)} \right] \quad (27)$$

For topological insulator

$$\frac{\text{Re } \sigma_+(\omega)}{\sigma_o} = \frac{2v_f^2 e \hbar B}{\pi} \left[\sum_{m=0}^{\infty} \left(\frac{[(A_{|m|+1} B_m)^2 \times \eta]}{(E_{|m|+1}^- - E_m^-)(\hbar\omega + E_m^- - E_{|m|+1}^-)^2 + \eta^2)} \right) + \right. \quad (28)$$

$$\left. \sum_{m=1}^{\infty} \left(\frac{(A_m B_{|m|-1})^2 \times \eta}{(E_{|m|-1}^+ - E_m^+)(\hbar\omega + E_m^+ - E_{|m|-1}^+)^2 + \eta^2} \right) \right]$$

and

$$\frac{\text{Re } \sigma_-(\omega)}{\sigma_o} = \frac{2v_f^2 e \hbar B}{\pi} \left[\sum_{m=0}^{\infty} \left(\frac{[(A_{|m|+1} B_m)^2 \times \eta]}{(E_{|m|+1}^+ - E_m^+)(\hbar\omega + E_m^+ - E_{|m|+1}^+)^2 + \eta^2)} \right) + \right. \quad (29)$$

$$\left. \sum_{m=1}^{\infty} \left(\frac{(A_m B_{|m|-1})^2 \times \eta}{(E_{|m|-1}^- - E_m^-)(\hbar\omega + E_m^- - E_{|m|-1}^-)^2 + \eta^2} \right) \right]$$

Fig. 12 shows absorption peaks for right handed circularly polarized light for $\text{Re } \sigma_+(\omega)/\sigma_o$ v.s. ω . The right handed circularly polarized light in normal insulator phase only gives $m \rightarrow |m| + 1$ transition for $\tau_z = -1$ and $m \rightarrow |m| - 1$ transition for $\tau_z = +1$. In both cases $m \leq -1$ if $\mu = 0$ while for topological insulator phase it gives $m \rightarrow |m| + 1$ transition for $\tau_z = -1$ with $m \leq 0$ for $\mu = 0$ and for $\tau_z = +1$ it gives $m \rightarrow |m| - 1$ transition with $m \leq -1$. The plot for topological insulator phase is shown in Fig. 12(a).

Fig. 13 shows absorptive peaks resulted from the left handed circularly polarized light for $\text{Re } \sigma_-(\omega)/\sigma_o$ v.s. ω . Left handed circularly polarized light gives $m \rightarrow |m| + 1$ for $\tau_z = +1$ and $m \rightarrow |m| - 1$ for $\tau_z = -1$ transitions with $m \leq 0$ for $\mu = 0$ in both cases. While in topological insulator it gives $m \rightarrow |m| + 1$ for $\tau_z = +1$ with $m \leq 0$ and $m \rightarrow |m| - 1$ for $\tau_z = -1$ transition with $m \leq -1$ for $\mu = 0$.

VI. SEMICLASSICAL LIMIT

The semiclassical limit is valid when the quantization between Landau levels is unimportant. It is the case when chemical potential $\mu \gg E_1$ [12]. For large μ all transitions will be intraband. The energy of intraband transitions is given by $\delta E = E_{n+1} - E_n$, which is approximated to give

$$\delta E = \frac{\hbar v_f^2 e B}{\sqrt{2N \hbar v_f^2 e B + (\Delta_Z \pm \Delta_H)}} \quad (30)$$

The chemical potential μ falls exactly between N and $N + 1$ with $N \gg 1$, so we can write $\mu \approx E_N$, we obtain

$$\delta E = \frac{\hbar v_f^2 e B}{\mu}, \quad (31)$$

so for n to $n + 1$ transitions the $\text{Re}\sigma_{xx}(\omega)$ in semiclassical limit is written as

$$\frac{\text{Re}\sigma_{xx}(\omega)}{\sigma_o} = \frac{\mu}{2\pi} \sum_{\tau_z=\pm 1, m} (A_{|m|+1} B_m)^2 \times \frac{\eta}{[(\hbar\omega - \frac{\hbar v_f^2 e B}{\mu})^2 + \eta^2]}.$$

The real part of the frequency dependent longitudinal optical conductivity $\text{Re}\sigma_{xx}(\omega)$ versus $\hbar\omega$ in units of e^2/h in the semiclassical limit is shown in Fig. 14 with $E_n < \mu < E_{n+1}$. The first pair starting from right side represents the transition between $n = 5$ to $n = 6$ while the 2nd pair represents the transition between $n = 11$ and $n = 12$ LLs and the last pair at the lowest energy represents the transition between $n = 20$ and $n = 21$ LLs. The dashed peak gives the transition between $\tau_z = -1$ LLs and solid peaks represent transitions for $\tau_z = +1$ LLs. We observe that as the chemical potential increases the spectral weight increases.

VII. BROKEN INVERSION SYMMETRIC TI THIN FILM

Thin film TIs are usually grown on a substrate which breaks inversion symmetry. In this case, the effective Hamiltonian in the symmetric and antisymmetric basis, Eq. (1), will be augmented by a term $V\sigma_x$ that breaks inversion symmetry. V represents the magnitude of inversion asymmetry. The Hamiltonian becomes

$$\hat{H}_{\sigma\tau} = \sqrt{\frac{\hbar}{2}} \frac{v_f}{l_B} (i\sigma_x(a^\dagger - a) + \tau_z \sigma_y(a + a^\dagger)) + (\Delta_Z \tau_z + \Delta_H) \sigma_z + V\sigma_x. \quad (32)$$

This is the inversion symmetry broken thin TI Hamiltonian given in Eq. (3) of [11], without the exchange field for ferromagnetic ordering but including an applied magnetic field. The single-particle eigenstates of the above Hamiltonian have the following form:

$$\begin{aligned} | |n\rangle \tau_z \text{sgn}(n) \rangle &= u_{n\tau_z=+1}^{\text{sgn}(n)} | |n| - 1, \uparrow, \tau_z = +1 \rangle + u_{n\tau_z=+1}^{\text{sgn}(n)} | |n|, \downarrow, \tau_z = +1 \rangle \\ &+ u_{n\tau_z=-1}^{\text{sgn}(n)} | |n|, \uparrow, \tau_z = -1 \rangle + u_{n\tau_z=-1}^{\text{sgn}(n)} | |n| - 1, \downarrow, \tau_z = -1 \rangle. \end{aligned} \quad (33)$$

$u_{n\tau_z}^{sgn(n)}$ are the complex four-component spinor wave functions. The Landau level spectrum can be obtained by diagonalizing the following Hamiltonian

$$\begin{pmatrix} \Delta_Z + \Delta_H & -i\sqrt{2\hbar n}\frac{v_f}{l_B}a & 0 & V \\ i\sqrt{2\hbar n}\frac{v_f}{l_B} & (\Delta_Z + \Delta_H) & V & 0 \\ 0 & V & -(\Delta_Z - \Delta_H) & i\sqrt{2\hbar n}\frac{v_f}{l_B}a^\dagger \\ V & 0 & -i\sqrt{2\hbar n}\frac{v_f}{l_B}a & \Delta_Z - \Delta_H \end{pmatrix} \quad (34)$$

Diagonalizing Eq. (34), we find the following LL spectrum:

$$E_n^{\tau_z} = sgn(n)\sqrt{2\hbar v_f^2 eB |n| + V^2 + \Delta_Z^2 + \Delta_H^2 + \tau_z 2\sqrt{2V^2\hbar v_f^2 eB |n| + V^2\Delta_Z^2 + \Delta_Z^2\Delta_H^2}} \quad (35)$$

$$E_0^{\tau_z} = -(\Delta_Z + \tau_z\sqrt{\Delta_H^2 + V^2}). \quad (36)$$

In the inversion symmetry broken system, the phase transition from normal insulator to topological insulating phase now occurs at $\Delta_Z = \sqrt{\Delta_H^2 + V^2}$. This shows that the phase transition is pushed to higher magnetic fields. For $V = 0$ the system is decoupled for $\tau_z = \pm 1$. As a result of inversion symmetry breaking, symmetric and antisymmetric hybridized states become coupled to each other and there can be allowed transitions between them. An additional feature is that broken inversion symmetry gives rise to crossing of LLs n with $\tau_z = +1$ and $n + 1$ with $\tau_z = -1$ at certain values of magnetic field, as shown in Fig. 15. This will allow additional transitions between LLs with $\tau_z = +1$ and LLs with $\tau_z = -1$. Recently, one photon and two photon absorption was investigated in topological insulator thin films with broken inversion symmetry [41], in the absence of a magnetic field. It was observed that additional transition channels open when inversion symmetry is not present.

VIII. EFFECT OF HEXAGONAL WARPING ON LANDAU LEVELS AND MAGNETO-OPTICAL CONDUCTIVITY

ARPES data suggests that there is warping effect on the band structure of Bi_2Te_3 . To take this effect into account, Fu[42] added a cubic correction term in the Hamiltonian of a topological insulator. This induces an anisotropic effect on the bands in momentum space whose strength is set by the parameter λ . The Hamiltonian of TI thin film in a magnetic

field with a warping term is

$$\hat{H}'_{\sigma\tau} = \hat{H}_{\sigma\tau} - \frac{2\lambda\hbar^{3/2}}{l_B^3} [(a^\dagger)^3 + (a)^3] \sigma_z \tau_z, \quad (37)$$

where $\hat{H}_{\sigma\tau}$ is given in Eq. (3). Analytical diagonalization of the above Hamiltonian is not possible. However, if warping is treated as a perturbation, then effect of warping on Landau levels can be evaluated[43]. These results show that the primary effect of warping on the LL spectrum is that slope of LLs increases with increasing magnetic field. This has implications on our work; warping affects the gap between LLs with optical transitions shifting to higher $\hbar\omega$. This effect will be more significant at higher magnetic fields.

IX. SUMMARY AND CONCLUSIONS

We have studied the effect of hybridization between the top and bottom surface states on the magneto-optical conductivity in a thin film TI. Hybridization induces gap in the Dirac spectrum. Each LL splits into two with the same Landau index representing LLs for symmetric and antisymmetric hybridized states. At a critical magnetic field the system makes a quantum phase transition from the NI phase to a TI phase. This has a signature in the magneto-optical absorption spectra, both $\text{Re } \sigma_{xx}(\omega)$ and $\text{Im } \sigma_{xy}(\omega)$. $\text{Re } \sigma_{xx}(\omega)$ peak for $E_{-1}^- \rightarrow E_0^-$ transition in NI phase is replaced by $E_0^- \rightarrow E_1^-$ peak in TI phase. More significant signature for the quantum phase transition is found in absorption spectra for $\text{Im } \sigma_{xy}(\omega)$. It shows negative peaks in the TI phase which are absent in the absorption spectra in NI phase. The signature in circularly polarized light is the splitting and shifting of the absorption peaks in TI phase relative to the NI phase.

X. ACKNOWLEDGEMENT

A. Ullah and K. Sabeeh acknowledge the support of Higher Education Commission (HEC) of Pakistan through project No. 20-1484/R&D/09. K. Sabeeh would also like to acknowledge the support of the Abdus Salam International Center for Theoretical Physics (ICTP) in

Trieste, Italy through the Associate Scheme where a part of this work was completed.

- [1] M. Z. Hasan and C. L. Kane, *Rev. Mod. Phys.* **82**, 3045 (2010).
- [2] X.-L. Qi and S.-C. Zhang, *Rev. Mod. Phys.* **83**, 1057 (2011).
- [3] D. Hsieh, et. al, *Nature (London)* **452**, 970 (2008).
- [4] Y. L. Chen, J. G. Analytiset al., *Science* **325**, 178 (2009).
- [5] D. Hsieh, et. al, *Nature (London)* **460**, 1101 (2009).
- [6] C. Jozwiak, X. L. Chenet al.,*Phys. Rev. B* **84**, 165113 (2011).
- [7] S.-Y. Xu, X. Xiaet al.,*Science* **332**, 560 (2011).
- [8] P. Ghaemi, R. Mong, and J.E. Moore, *Phys. Rev. Lett.* **105**, 166603 (2010).
- [9] H.-Z. Lu, W.-Y. Shan, W. Yao, Q. Niu, and S.-Q. Shen, *Phys. Rev. B* **81**, 115407 (2010).
- [10] C.-X. Liu, H. Zhang, B. Yan, X.-L. Qi, T. Frauenheim, X. Dai, Z. Fang, and S.-C. Zhang, *Phys. Rev. B* **81**, 041307(R) (2010).
- [11] R. Yu, W. Zhang, H.-J. Zhang, S.-C. Zhang, X. Dai, and Z. Fang,*Science* **329**, 61 (2010).
- [12] B. Seradjeh, J.E. Moore, and M. Franz, *Phys. Rev. Lett.* **103**, 066402 (2010).
- [13] Y. Zhang, K. He, C. Z. Chang, C. L. Song, L. L. Wang, X. Chen, J. F. Jia, Z. Fang, X. Dai, W. Y. Shan, S. Q. Shen, Q. Niu, X. L. Qi, S. C. Zhang, X. C. Ma, and Q. K. Xue, *Nat. Phys.* **6**, 584 (2010).
- [14] H. Cao, J. Tian, I. Miotkowski, T. Shen, J. Hu, S. Qiao, and Y. P. Chen, *Phys. Rev. Lett.* **108**, 216803 (2012).
- [15] C. X. Liu, H. Zhang, B. Yan, X. L. Qi, T. Frauenheim, X. Dai, Z. Fang, and S. C. Zhang, *Phys. Rev. B* **81**, 041307 (2010).
- [16] G. Zhang, H. Qin, J. Teng, J. Guo, Q. Guo, X. Dai, Z. Fang, and K. Wu, *Appl. Phys. Lett.* **95**, 053114 (2009).
- [17] P. Cheng, C. Song, T. Zhang, Y. Zhang, Y. Wang, J. F. Jia, J. Wang, Y. Wang, B. F. Zhu, X. Chen, X. Ma, K. He, L. Wang, X. Dai, Z. Fang, X. Xie, X. L. Qi, C. X. Liu, S. C. Zhang, and Q. K. Xue, *Phys. Rev. Lett.* **105**, 076801 (2010).
- [18] J. Wang, A. M. DaSilva, C. Z. Chang, K. He, J. K. Jain, N. Samarth, X. C. Ma, Q. K. Xue, and M. H. W. Chan, *Phys. Rev. B* **83**, 245438 (2011).
- [19] Jacob Linder, Takehito Yokoyama, and Asle Sudbo, *Phys. Rev. B* **80**, 205401 (2009).

- [20] A. A. Zyuzin, M. D. Hook, and A. A. Burkov, *Phys. Rev. B* **83**, 245428 (2011).
- [21] A. A. Zyuzin and A. A. Burkov, *Phys. Rev. B* **83**, 195413 (2011).
- [22] M. Tahir, K. Sabeeh, and U. Schwingenschlöggl *J. Appl. Phys.* **113**, 043720 (2013)
- [23] Y. L. Chen, J. G. Analytis et.al, *Science* **325**, 178 (2009).
- [24] V. P. Gusynin, S. G. Sharapov, and J. P. Carbotte, *Phys. Rev. Lett.* **98**, 157402 (2007).
- [25] V. P. Gusynin, S. G. Sharapov, and J. P. Carbotte, *New J. Phys.* **11**, 095013 (2009).
- [26] Z. Li, E. A. Henniksen et al., *Nat. Phys.* **4**, 532 (2008).
- [27] E. J. Nicol and J. P. Carbotte, *Phys. Rev. B* **77**, 155409 (2008).
- [28] T. Stauber and N. M. R. Peres, *J. Phys.: Condens. Matter* **20**, 055002 (2008).
- [29] M. Lasia and L. Brey, *Phys. Rev. B* **90**, 075417(2014)
- [30] Zhou Li and J. P. Carbotte *Phys. Rev. B* **88**, 045414 (2013).
- [31] Zhou Li and J. P. Carbotte, *Phys. Rev. B* **86**, 205425 (2012).
- [32] Zhou Li and J. P. Carbotte, *Physica B* **421**, 97 (2013).
- [33] L. Stille, C. J. Tabert, and E. J. Nicol, *Phys. Rev. B* **86**, 195405 (2012).
- [34] V. P. Gusynin, S. G. Sharapov, and J. P. Carbotte, *J. Phys.: Condens. Matter* **19**, 026222 (2007).
- [35] A. Pound, J. P. Carbotte and E. J. Nicol, *Phys. Rev. B* **85**, 125422 (2012).
- [36] C. J. Tabert and E. J. Nicol, *Phys. Rev. Lett.* **110**, 197402 (2013).
- [37] C. J. Tabert and E. J. Nicol, *Phys. Rev. B* **88**, 085434 (2013).
- [38] C. X. Liu, X. L. Qi, H. Zhang, X. Dai, Z. Fang, and S. C. Zhang *Phys. Rev. B* **82**, 045122 (2010).
- [39] G. D. Mahan *Many-Particle Physics*, Third Edition, Kluwer Academic/Plenum Publishers (2000).
- [40] N. P. Butch, K. Kirshenbaum, P. Syers, A. B. Sushkov, G. S. Jenkins, H. D. Drew, and J. Paglione *Phys. Rev. B* **81**, 241301(R) (2010).
- [41] J. Wang, H. Mabuchi, and X-L. Qi, *Phys. Rev. B* **88**, 195127 (2013).
- [42] L. Fu, *Phys. Rev. Lett.* **103**, 266801 (2009).
- [43] E.V. Repin, V.S. Stolyarov, T. Cren, C. Brun, S.I. Bozhko, L.V. Yashina, D. Roditchev, and I.S. Burmistrov, arXiv:1408.6960 (2014).

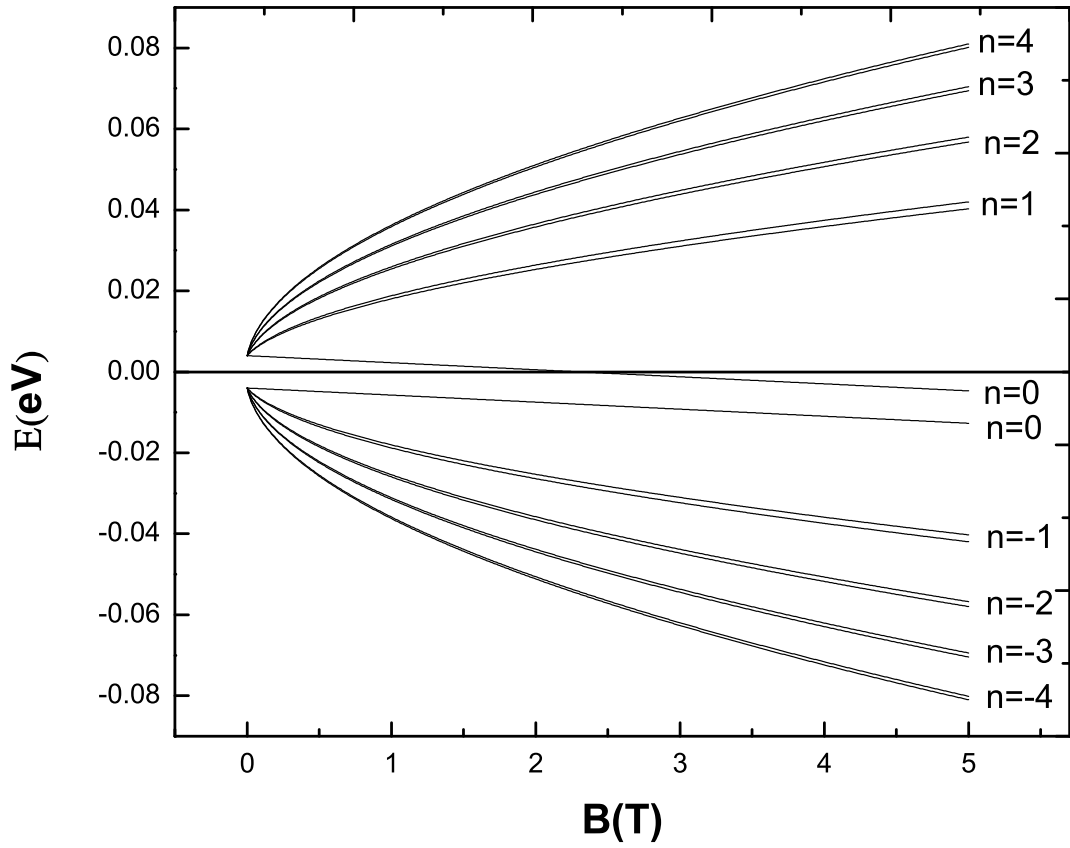


FIG. 1: Landau level energies as a function of magnetic field(B) in units of Tesla with hybridization energy $\Delta_H = 0.004\text{eV}$ and Zeeman energy $\Delta_Z = 0.00174 \times B \frac{\text{eV}}{\text{T}}$.

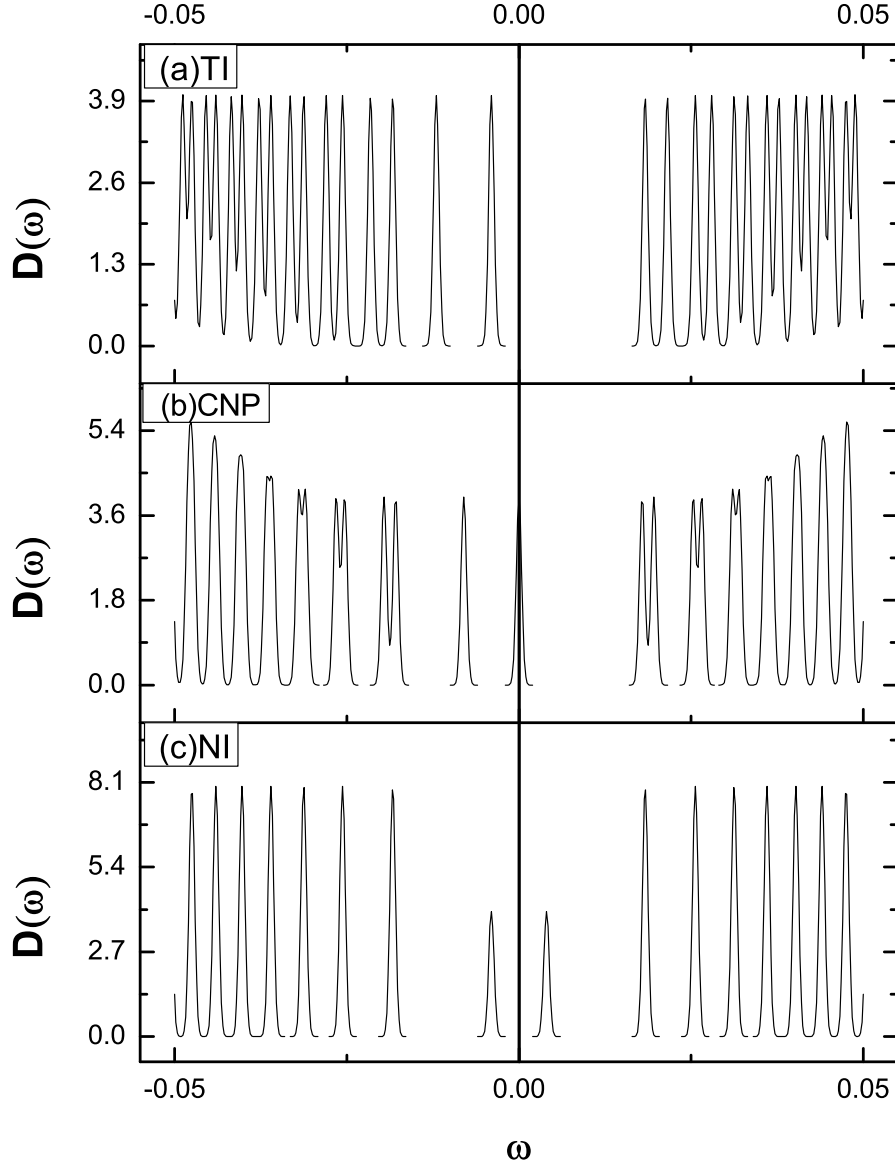


FIG. 2: Density of states for thin film topological insulator in a magnetic field in units of $eB/2\pi\hbar$. (a) Density of states in topological insulator phase ($\Delta_Z < \Delta_H$) (b) Density of states at charge neutrality point ($\Delta_Z = \Delta_H$). (c) Density of states in normal insulator phase ($\Delta_Z > \Delta_H$).

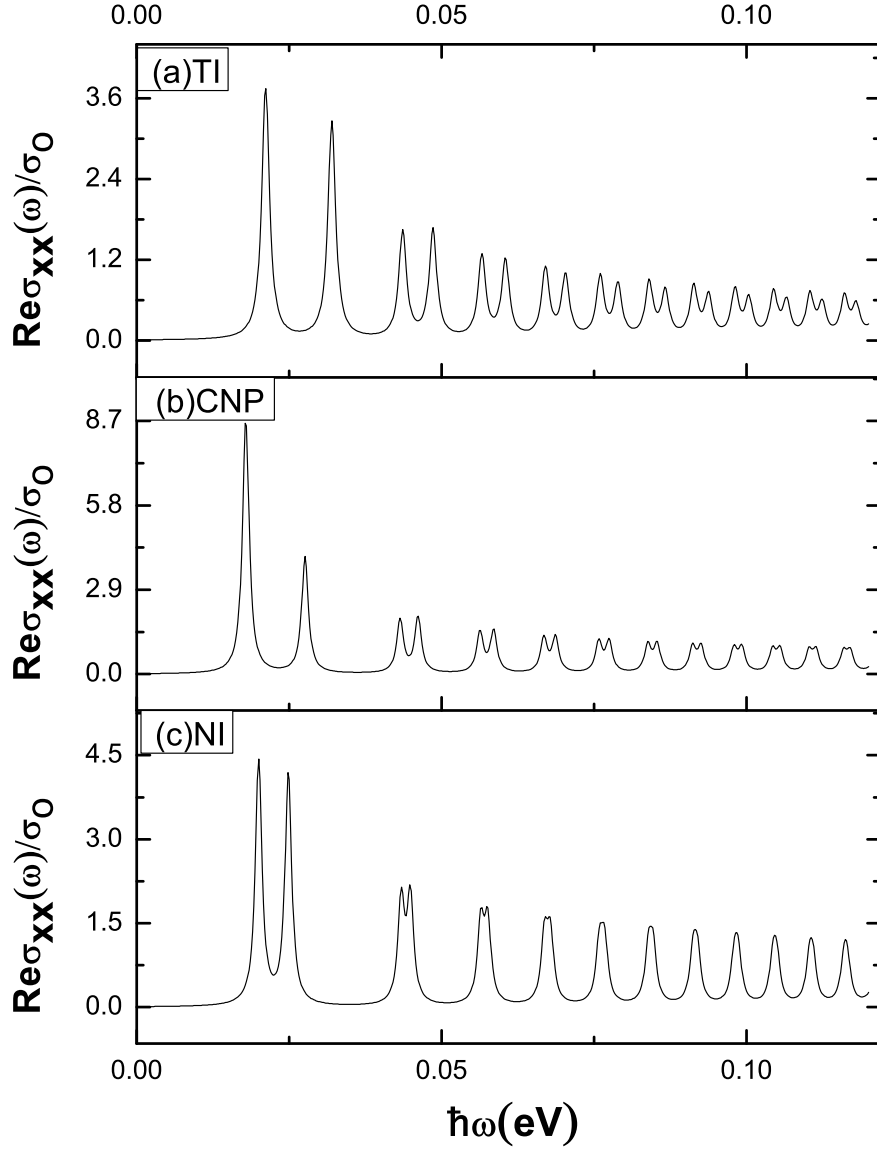


FIG. 3: Real part of the longitudinal conductivity $\sigma_{xx}(\omega)$ of thin film topological insulator in units of e^2/\hbar as a function of $\hbar\omega$ in eV compared in (a) topological insulator phase, (b) CNP and (c) normal insulator phase. The scattering rate is $\eta = 0.15\Delta_H$ and $\mu = 0$.

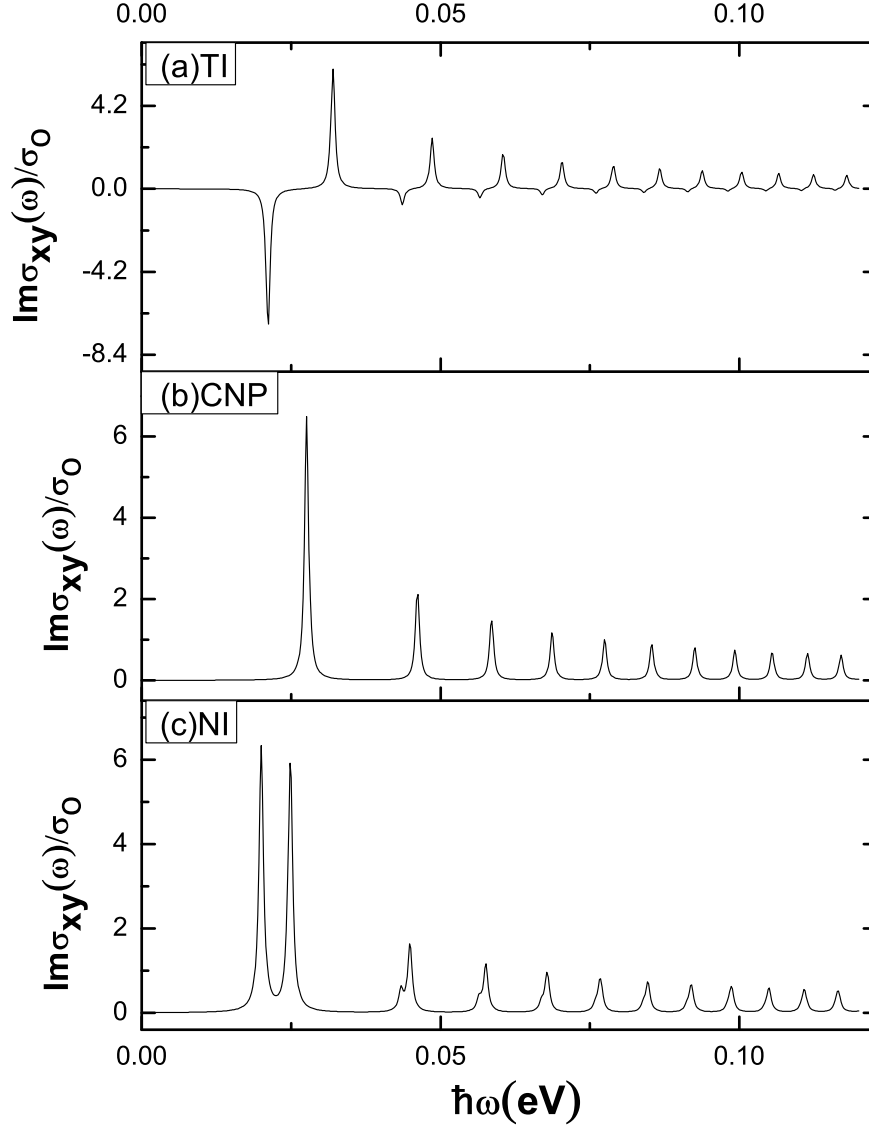


FIG. 4: Imaginary part of the transverse conductivity $\sigma_{xy}(\omega)$ of thin film topological insulator in units of e^2/\hbar as a function of $\hbar\omega$ in eV compared in (a) topological insulator phase, (b) CNP and (c) normal insulator phase. The scattering rate is $\eta = 0.15\Delta_H$ and $\mu = 0$.

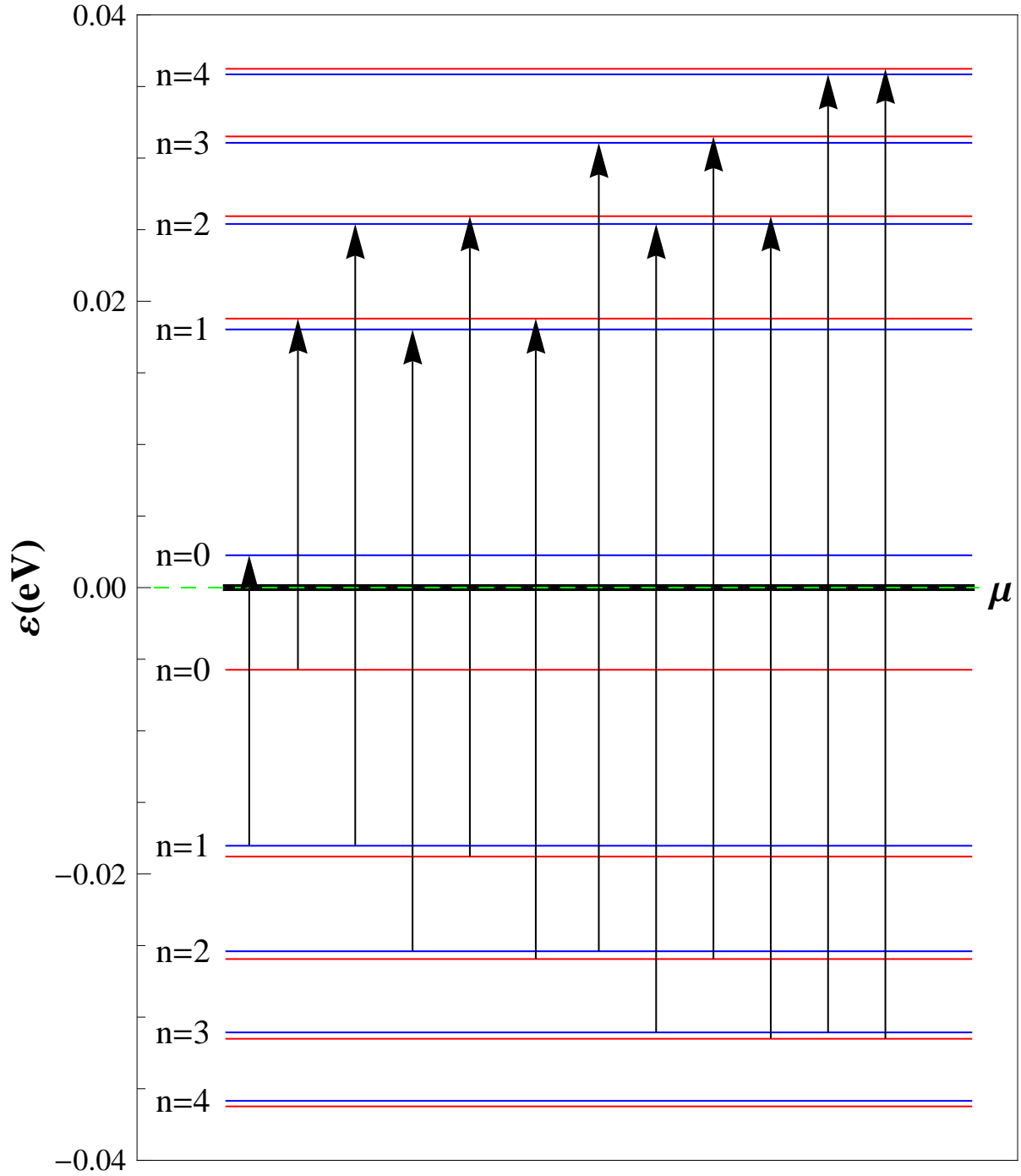


FIG. 5: Schematic representation of the allowed transitions between Landau level of same τ_z in normal insulator phase for $\mu = 0$. Blue lines represent Landau levels for $\tau_z = -1$ and red lines represent Landau levels for $\tau_z = +1$.

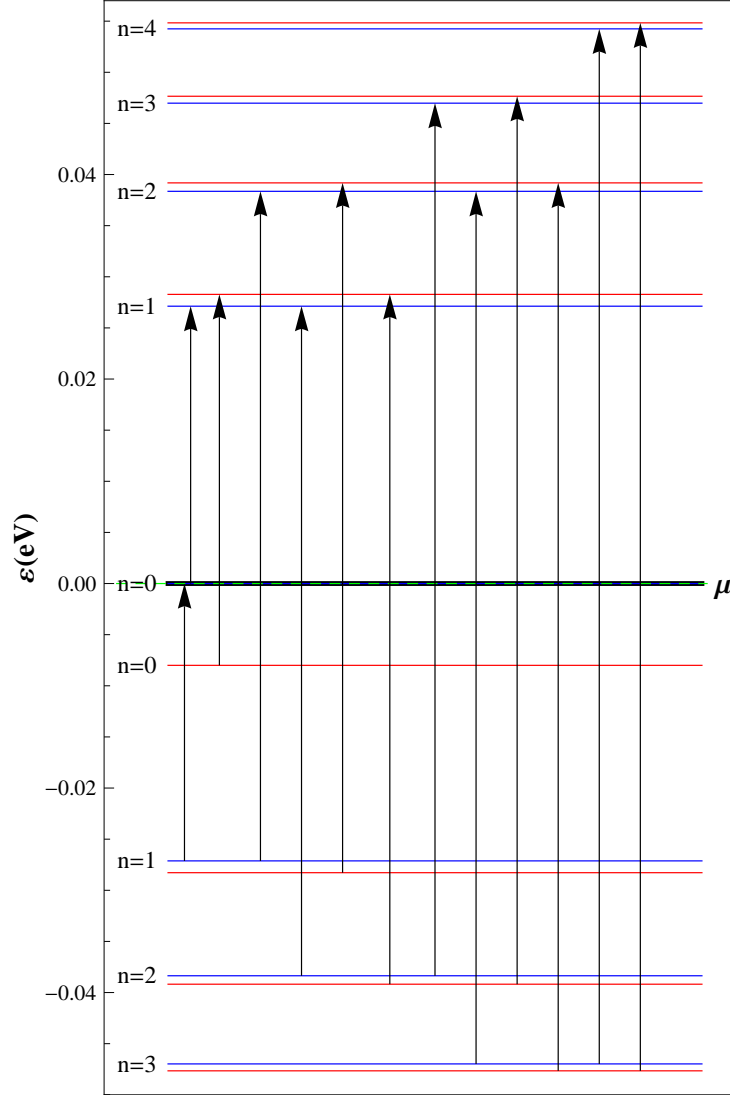


FIG. 6: Schematic representation of the allowed transitions between Landau level of same τ_z at CNP $\mu = 0$. Blue lines represent Landau levels for $\tau_z = -1$ and red lines represent Landau levels for $\tau_z = +1$.

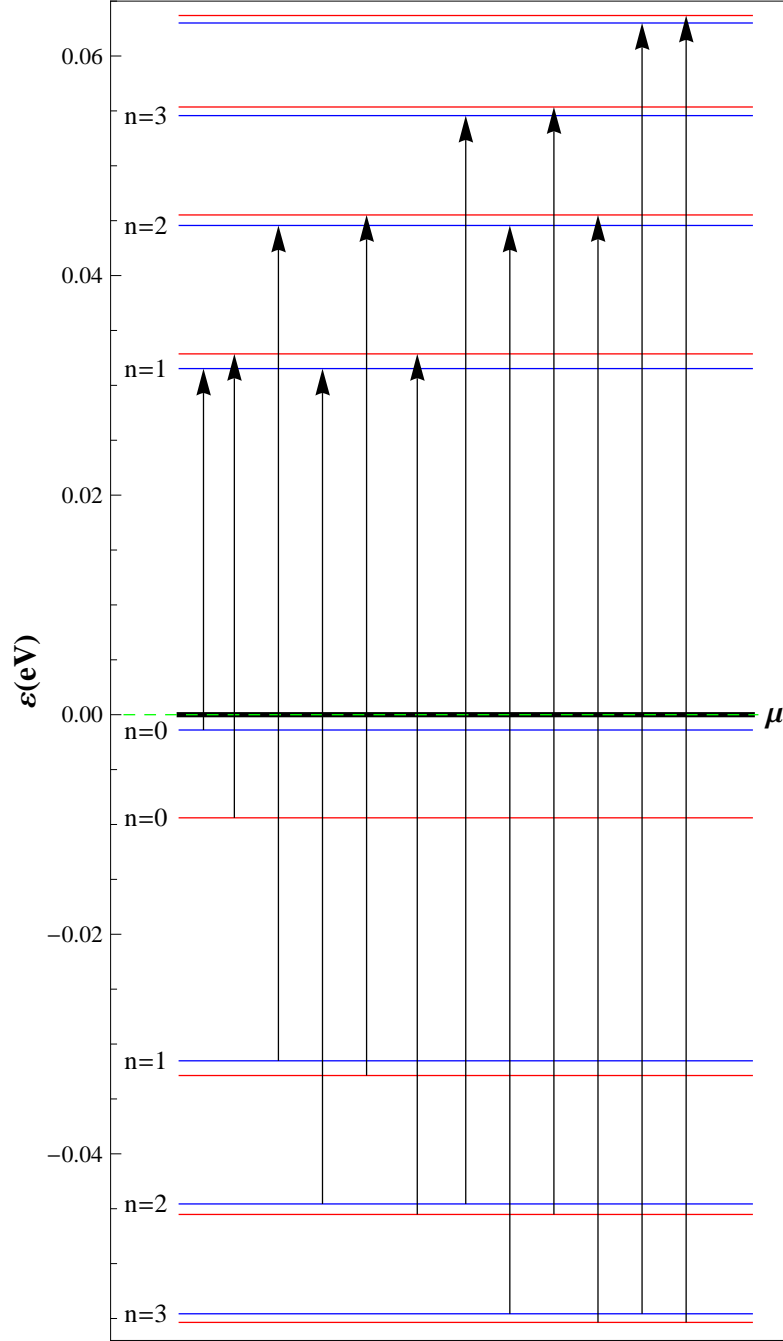


FIG. 7: Schematic representation of the allowed transitions between Landau level of same τ_z in topological insulator phase. Blue lines represent Landau levels for $\tau_z = -1$ and red lines represent Landau levels for $\tau_z = +1$.

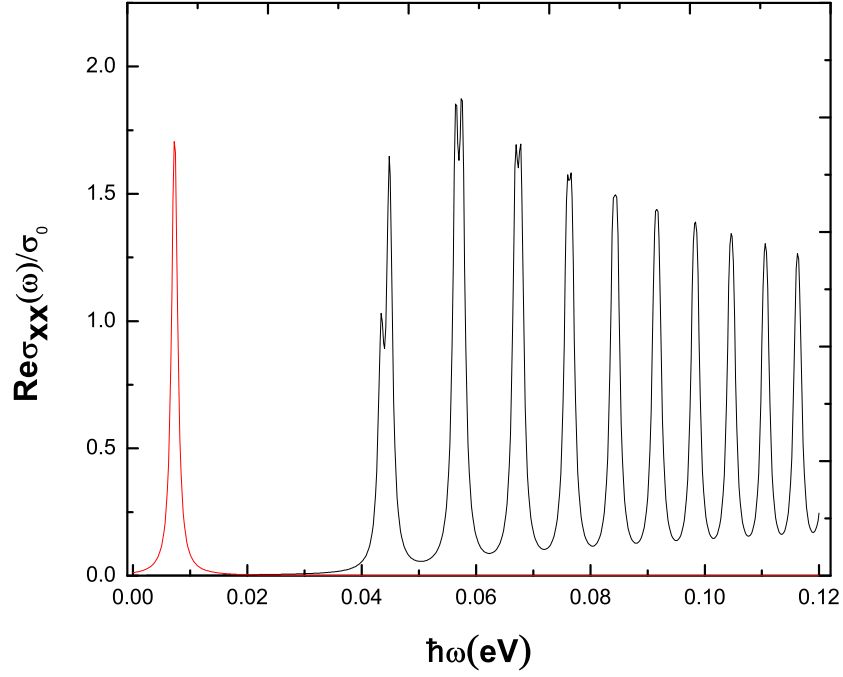


FIG. 8: Real part of the longitudinal conductivity $\sigma_{xx}(\omega)$ of thin film topological insulator in units of e^2/\hbar as a function of $\hbar\omega$ in eV in normal insulator phase. The scattering rate is $\eta = 0.15\Delta_H$ and $\mu = 0.0225$ and $B = 2T$. Red peak represents absorption peak for intraband transition while black peaks represent absorption peaks for interband transitions.

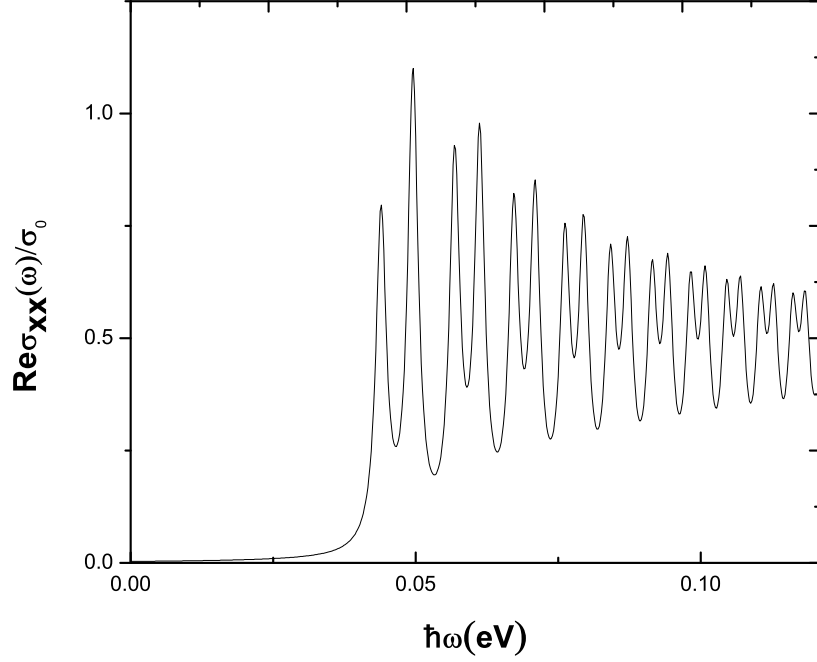


FIG. 9: Real part of the longitudinal conductivity $\sigma_{xx}(\omega)$ of thin film topological insulator in units of e^2/\hbar as a function of $\hbar\omega$ in eV in topological insulator phase. The scattering rate is $\eta = 0.15\Delta_H$, $\mu = 0.0225$ and $B = 4T$. All peaks represent absorption peaks for interband transitions.

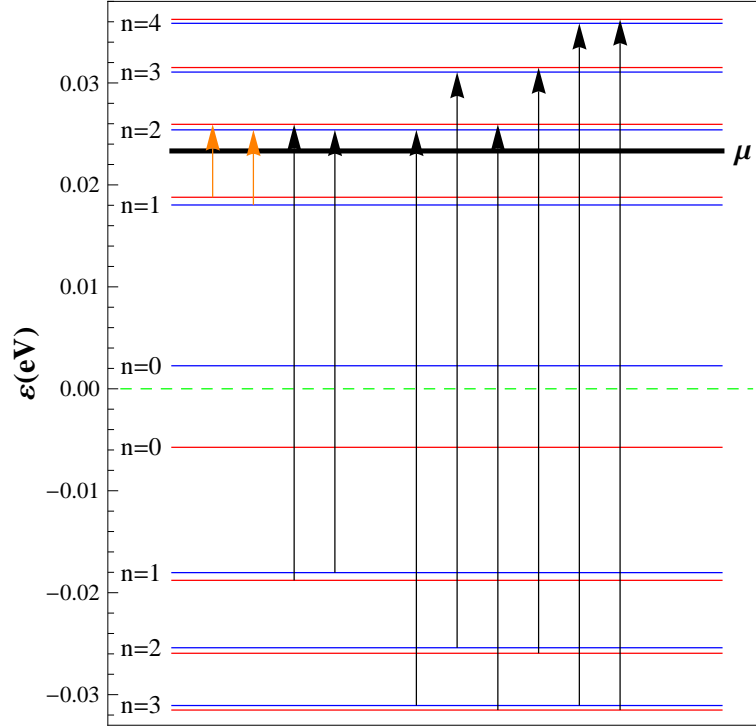


FIG. 10: Schematic representation of the allowed transitions between Landau levels of same τ_z in normal insulator phase for $B = 1T$ and $\mu = 0.02eV$. Orange arrows represent intraband transition and black arrows represent interband transitions.

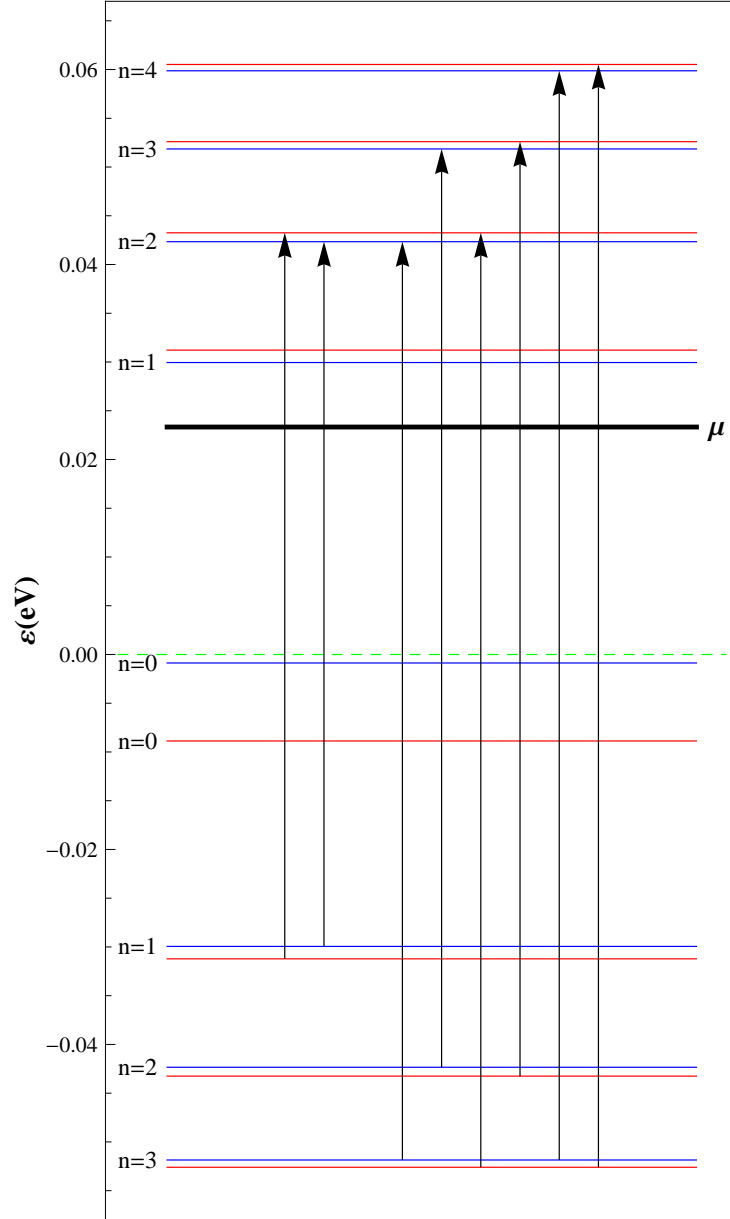


FIG. 11: Schematic representation of the allowed transitions between Landau level of same τ_z in topological insulator phase with $B = 3T$ and $\mu = 0.02eV$.

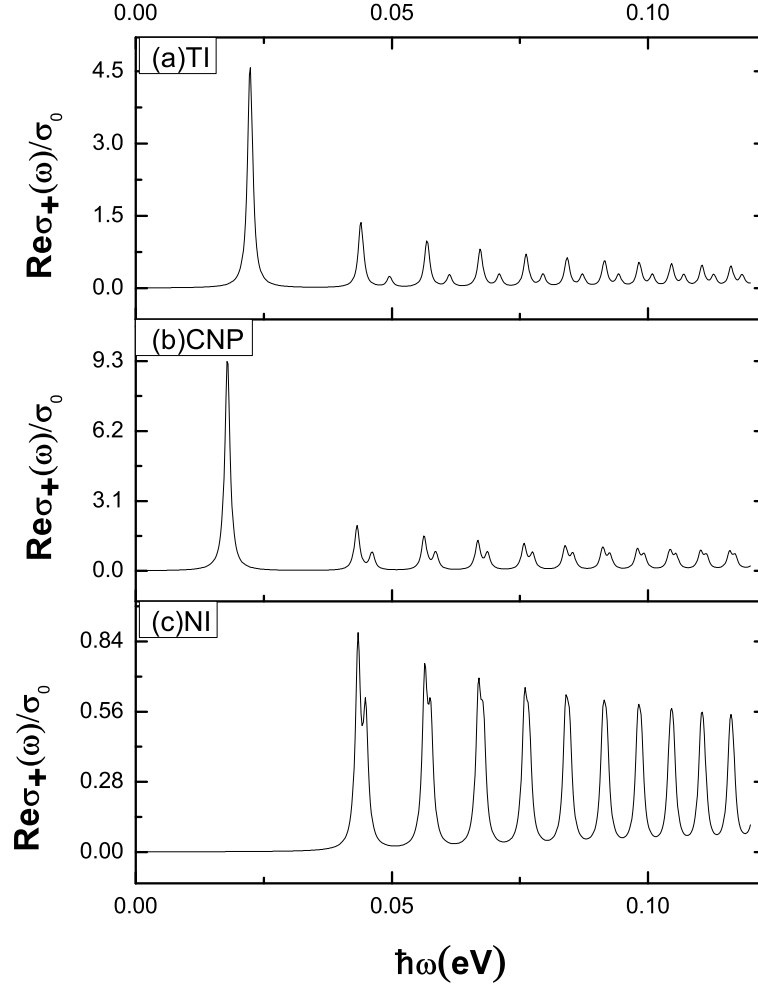


FIG. 12: $\text{Re}\sigma_+(\omega)/\sigma_0$ as a function of frequency for right handed circularly-polarized light in (a) topological insulator phase (b) at CNP (c) normal insulator phase.

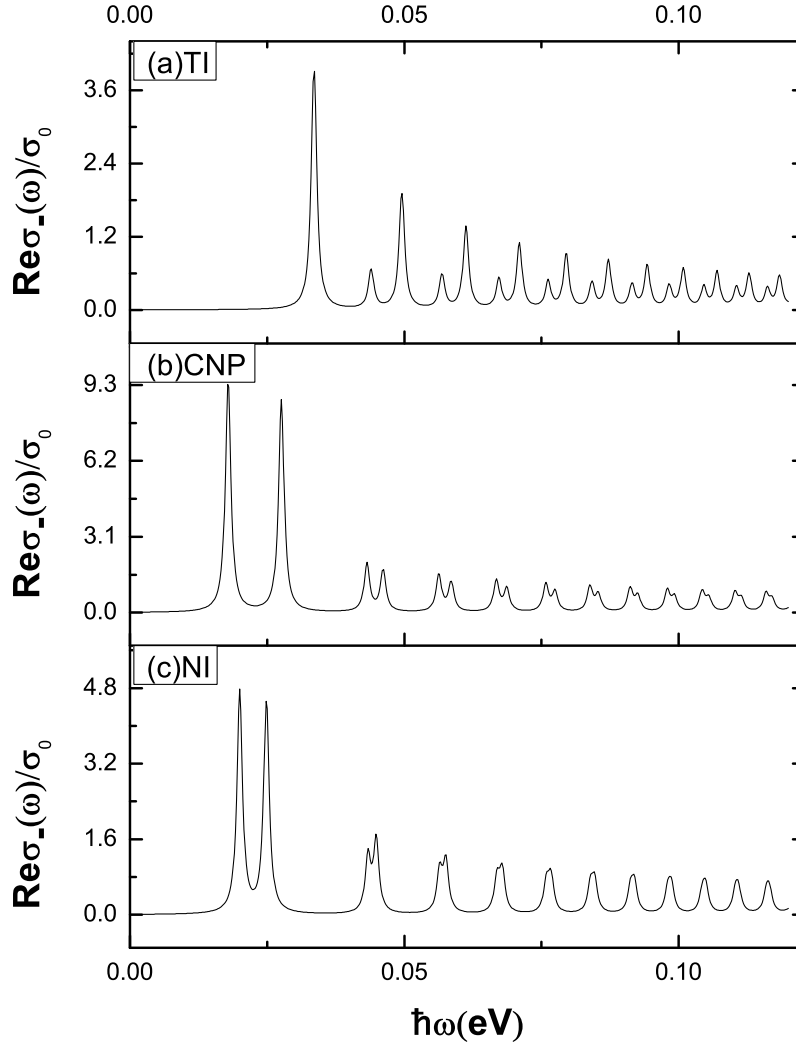


FIG. 13: $Re\sigma_{-}(\omega)/\sigma_o$ as a function of frequency for left handed circularly-polarized light in (a) topological insulator phase (b) at CNP (c) normal insulator phase.

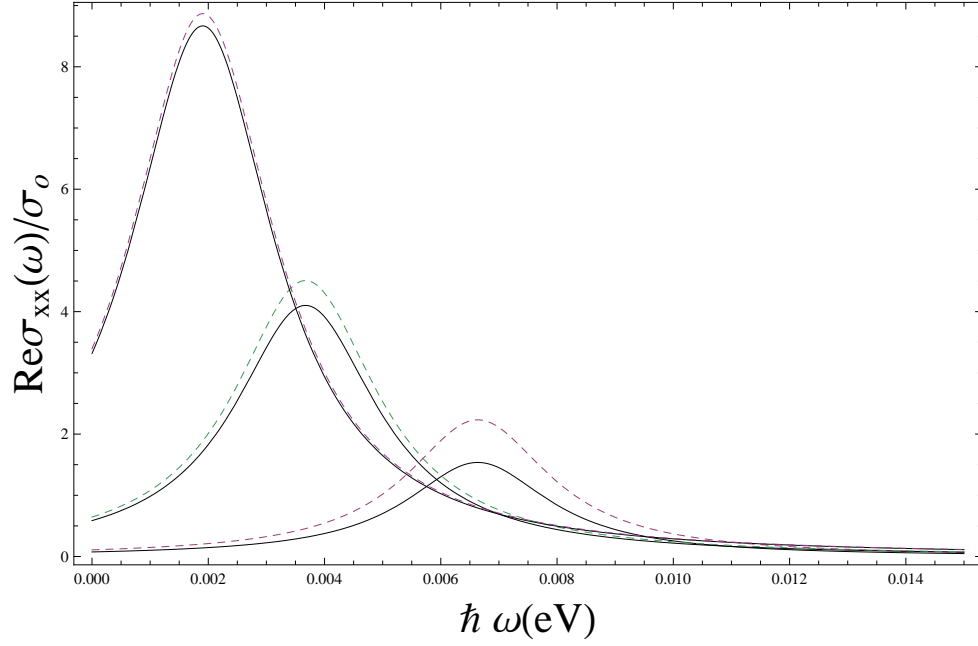


FIG. 14: The semiclassical limit of the real part of the longitudinal conductivity $\text{Re} \sigma_{xx}(\omega)/\sigma_o$ in units of e^2/\hbar in eV.

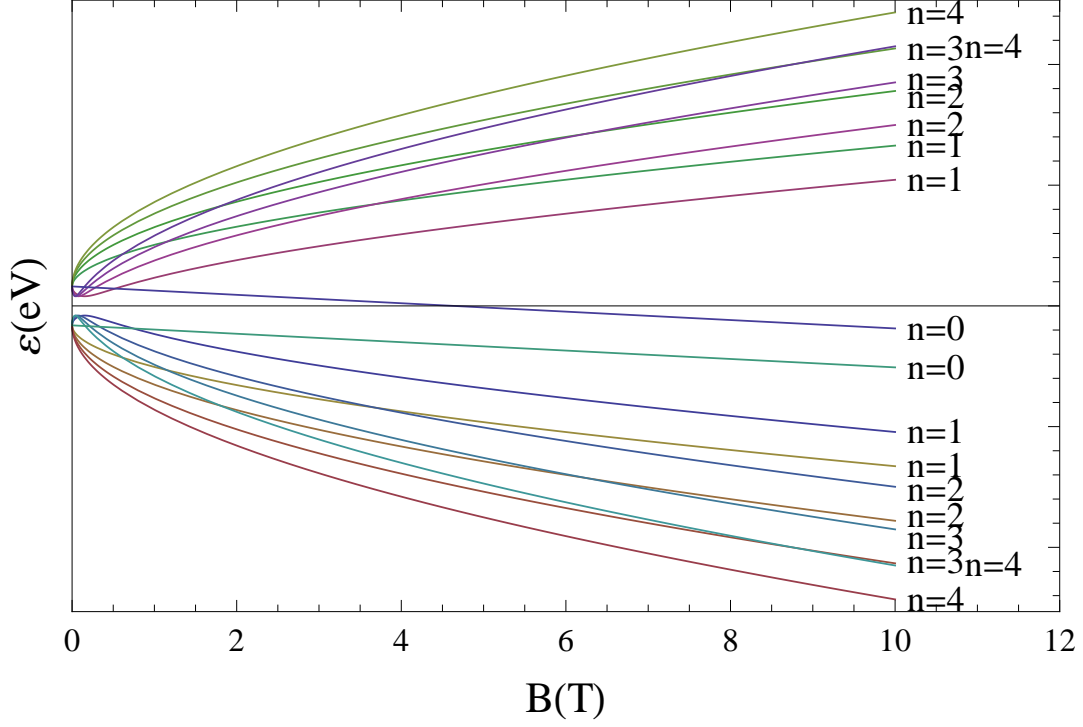


FIG. 15: Landau levels energies for broken inversion symmetric TI as a function of magnetic field(B) in units of Tesla with hybridization energy $\Delta_H = 0.004eV$, Zeeman energy $\Delta_Z = 0.00174 \times B \frac{eV}{T}$ and $V = 0.006eV$.